

## Spatially modulated magnetic structure of EuS due to the tetragonal domain structure of SrTiO<sub>3</sub>

Aaron J. Rosenberg,<sup>1,\*</sup> Ferhat Katmis,<sup>2,3,4</sup> John R. Kirtley,<sup>1</sup> Nuh Gedik,<sup>3</sup> Jagadeesh S. Moodera,<sup>2,3</sup> and Kathryn A. Moler<sup>1,5,6</sup>

<sup>1</sup>*Department of Applied Physics, Stanford University, Stanford, California 94305, USA*

<sup>2</sup>*Francis Bitter Magnetic Laboratory, Massachusetts Institute of Technology, 77 Massachusetts Avenue, Cambridge, Massachusetts 02139, USA*

<sup>3</sup>*Department of Physics, Massachusetts Institute of Technology, 77 Massachusetts Avenue, Cambridge, Massachusetts 02139, USA*

<sup>4</sup>*Department of Physics, Middle East Technical University, 06800, Ankara, Turkey*

<sup>5</sup>*Department of Physics, Stanford University, Stanford, California 94305, USA*

<sup>6</sup>*Stanford Institute for Materials and Energy Sciences, SLAC National Accelerator Laboratory, 2575 Sand Hill Road, Menlo Park, California 94025, USA*

(Received 20 June 2017; published 15 December 2017)

The combination of ferromagnets with topological superconductors or insulators allows for new phases of matter that support excitations such as chiral edge modes and Majorana fermions. EuS, a wide-bandgap ferromagnetic insulator with a Curie temperature around 16 K, and SrTiO<sub>3</sub> (STO), an important substrate for engineering heterostructures, may support these phases. We present scanning superconducting quantum interference device measurements of EuS grown epitaxially on STO that reveal micron-scale variations in ferromagnetism and paramagnetism. These variations are oriented along the STO crystal axes and only change their configuration upon thermal cycling above the STO cubic-to-tetragonal structural transition temperature at 105 K, indicating that the observed magnetic features are due to coupling between EuS and the STO tetragonal structure. We speculate that the STO tetragonal distortions may strain the EuS, altering the magnetic anisotropy on a micron scale. This result demonstrates that local variation in the induced magnetic order from EuS grown on STO needs to be considered when engineering new phases of matter that require spatially homogeneous exchange.

DOI: [10.1103/PhysRevMaterials.1.074406](https://doi.org/10.1103/PhysRevMaterials.1.074406)

EuS is a well-studied wide-bandgap ferromagnetic insulator with a NaCl-type structure (lattice constant of 5.94 Å) and a bulk Curie temperature of 16.8 K [1–3]. It has historically been used as an efficient spin filter to spin-polarize charge currents. [4–9]. Because EuS is considered a simple Heisenberg ferromagnet (a ferromagnet that can orient in any three-dimensional (3D) direction [10]), it has long been considered a model system to test theories of magnetism [11–14]. EuS has been of recent interest because it may induce magnetic order in topologically nontrivial systems [15,16]. For example, 3D topologically insulating Bi<sub>2</sub>Se<sub>3</sub> [17–21] has been combined with EuS to induce high-temperature ferromagnetism in the Bi<sub>2</sub>Se<sub>3</sub> [22]. Additional potential applications include the creation of topological superconductivity to produce zero-energy Majorana fermion modes [23,24], the topological magnetoelectric effect [25,26], a magnetic monopole [27], and the quantum anomalous Hall effect [28,29]. In the latter example, one could grow a heterostructure of EuS/topological insulator/EuS with the intention of breaking time reversal symmetry on the top and bottom surface states in order to observe chiral edge modes [25].

SrTiO<sub>3</sub> (STO) is a common substrate for growing new heterostructures such as high-temperature superconductors [30–32], ferroelectrics [33,34], and electronic systems with high spin-orbit coupling [35]. STO is a perovskite band insulator with a cubic unit cell. Excitingly, it becomes an unconventional superconductor when doped [36,37], and the interface between STO and another perovskite band insulator, LaAlO<sub>3</sub>, is both conducting [38,39] and superconducting [40].

At 105 K, STO undergoes a cubic-to-tetragonal structural phase transition because of small rotations of the Ti-O octahedra that causes the unit cell to elongate along one of the crystallographic axes [41]. Without external strain, the STO unit cell can elongate along any of the original cubic axes forming structural domains separated by twin planes. In terms of the original cubic directions, the twin planes are along (110)<sub>p</sub>, (101)<sub>p</sub>, and (011)<sub>p</sub>. Recent studies have shown that the low-temperature twin structure affects both the interfacial conductivity in LaAlO<sub>3</sub>/SrTiO<sub>3</sub> heterostructures [42,43] and the superconducting transition temperature in STO [44].

We measured the magnetic spatial landscape in four EuS/STO-based heterostructures using a scanning superconducting quantum interference device (SQUID) susceptometer in a <sup>4</sup>He cryostat. Unless otherwise indicated, the data in this paper were taken on a thin film (5 nm) of (001)<sub>p</sub>-oriented EuS grown on a (001)<sub>p</sub>-oriented STO substrate, but we observed similar effects in samples with (110)<sub>p</sub>- and (111)<sub>p</sub>-oriented STO substrates and samples with 3-nm-thick EuS [45].

The SQUID sensor measures the total flux through the pickup loop, which is integrated with the body of the SQUID through well-shielded superconducting coaxial leads. The pickup loop size and height above the surface determine the spatial resolution. The pickup loop has an inner radius of 1 μm and an outer radius of 1.5 μm, resulting in an effective radius of 1.24 μm [46]. The pickup loop is centered in a single-turn field coil with a 2.5-μm inner radius that can be used to apply a local magnetic field to the sample. Using this sensor, we simultaneously probed the static ferromagnetism (magnetometry) as well as the susceptibility (susceptometry) of the sample [47]. Magnetometry imaging was carried out by measuring the magnetic flux through the SQUID pickup

\*rosenberg.aaronj@gmail.com

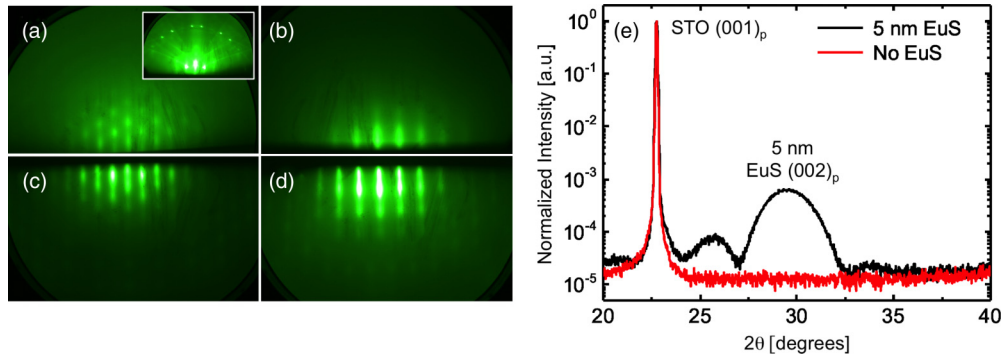


FIG. 1. Captured RHEED patterns of EuS after growth and annealing. RHEED snapshot taken with a 15-keV electron beam along (a) the  $[110]_p$  azimuth and (b) the  $[001]_p$  azimuth (c) after growth and (d) after annealing, respectively. (e) X-ray diffraction of the EuS/STO heterostructure (black line) and STO substrate without a EuS layer (red line). Besides the characteristic intense substrate reflection on the low-angle side, another reflection is visible around  $\simeq 29.5^\circ$ , which belongs to the  $(002)_p$  reflection of EuS. The representative data also show pronounced Laue oscillations (oscillations in the vicinity of the EuS Bragg peak), which indicate coherency of the top and the bottom surface parallelism of the epitaxial EuS layer.

loop, which is the  $z$  component of the magnetic field produced by the sample convolved with the pickup loop's point-spread function. Susceptometry involved applying a small alternating current (ac) to the field coil and recording the flux through the pickup loop using standard lock-in techniques [48]. To image, we fixed the SQUID sensor above the sample and rastered the sample in the  $x$ - $y$  plane using an attocube piezoelectric stack. We thermally coupled the SQUID sensor directly to the liquid helium bath, and we thermally isolated the sample and heater, allowing us to study the magnetic behavior of the sample at temperatures even higher than the superconducting transition temperature of the SQUID ( $T_C = 9$  K).

Epitaxial EuS growth and STO substrate preparation were performed in a custom-built molecular beam epitaxy system under a base pressure of  $2 \times 10^{-10}$  T. The system is equipped with ultrahigh-purity source materials for *in situ* growth and protection of the films, as well as units to monitor the thickness of the layer during growth. The interface formation and structural evolution of the grown layer were displayed via an *in situ* reflection high-energy electron diffraction (RHEED) apparatus. The STO epitaxial substrate was prepared *in situ* after several heat treatments to form an atomically flat surface, which was ensured via RHEED [Fig. 1(a), inset].

Due to the high reactivity of europium atoms and dissociation problems with sulfur, the EuS was evaporated congruently from a single electron-beam source. To avoid kinetic surface roughening, a growth rate of  $\simeq 1\text{--}3 \text{ \AA min}^{-1}$  was used to produce a quasismooth surface at 523–563 K. Layers were grown at 523 K and annealed after growth at 563 K until the layer quality was optimized, as determined via analysis of the RHEED pattern [Figs. 1(a) and 1(b)]. Even high-temperature growth does not provide sufficient surface mobility to the EuS molecules; therefore, surface roughening occurs above a critical thickness of 3–4 nm [15,22]. While the film was annealing after the growth [Figs. 1(c) and 1(d)], quasi-2D layer streaks transformed into mostly 2D modes, indicating surface smoothing after annealing, which helped to form a smooth EuS layer. As the final step, films were covered *in situ* with  $\simeq 5$  nm amorphous  $\text{Al}_2\text{O}_3$  at room temperature as a protection layer in the same deposition chamber.

In order to obtain detailed information on the crystal structure, the films were investigated by x-ray-based diffraction in addition to RHEED. A well-collimated nearly background-free beam is impinged on the sample surface and the scattered x-ray intensity is collected by a 2D CCD camera. The incoming beam is diffracted by a Ge (220) four-bounce crystal monochromator to get  $\text{CuK}\alpha_1$  radiation (wavelength  $\lambda = 1.54056 \text{ \AA}$ ) over a wide range of diffraction angles. The x-ray diffraction pattern at room temperature shows two major Bragg peaks in Fig. 1(e). The more intense peak corresponds to the substrate, while the less intense one at around  $\simeq 29.5^\circ$  corresponds to Bragg reflection from the 5-nm EuS ( $[002]_p$ ) layer, indicating that the substrate surface is parallel to the grown layer in the  $\text{STO}(001)_p/\text{EuS}(001)_p$  orientation. From this measurement we determine the  $(001)_p$  lattice constant to be 6.06  $\text{\AA}$ , which indicates a strain of  $\simeq 2\%$  from the known bulk lattice constant of 5.94  $\text{\AA}$ . Laue oscillations also occur near the layer's Bragg peak, which again indicates sharp surface/interface coherency. From these Laue oscillations, we can calculate the thickness ( $\approx 5$  nm) of the grown layer, which matches quite well to the thicknesses monitored by the quartz crystal sensor during growth.

We present representative magnetometry images [Figs. 2(a)–2(c)] of the spatial modulation of ferromagnetism [Fig. 2(d)] on the micron scale when the heterostructure was trained (cooled through the Curie transition) with a 13-G in-plane field. These scanning SQUID images were taken in the same cooldown at different locations on the sample. Note that the amplitude of the training field does not affect the features [45]. We defined the growth direction to be  $[001]_p$ . Unless indicated otherwise, the field training direction was pointed along the  $\text{STO}[\bar{1}00]_p$  axis with respect to the original STO cubic crystal axes. The modulated ferromagnetic landscape appears as magnetic striations oriented along the  $[110]_p$  direction [Fig. 2(a)], the  $[010]_p$  direction [Fig. 2(b)], and the  $[100]_p$  direction [Fig. 2(c)]. The crystal directions were determined by knowledge of the growth direction and calibrated by scanning the edge of the sample pointing along the  $[010]_p$  direction [Fig. 2(e)]. The STO twin planes that intersect with the surface are along the  $[100]_p$ ,  $[110]_p$ ,  $[\bar{1}\bar{1}0]_p$ ,

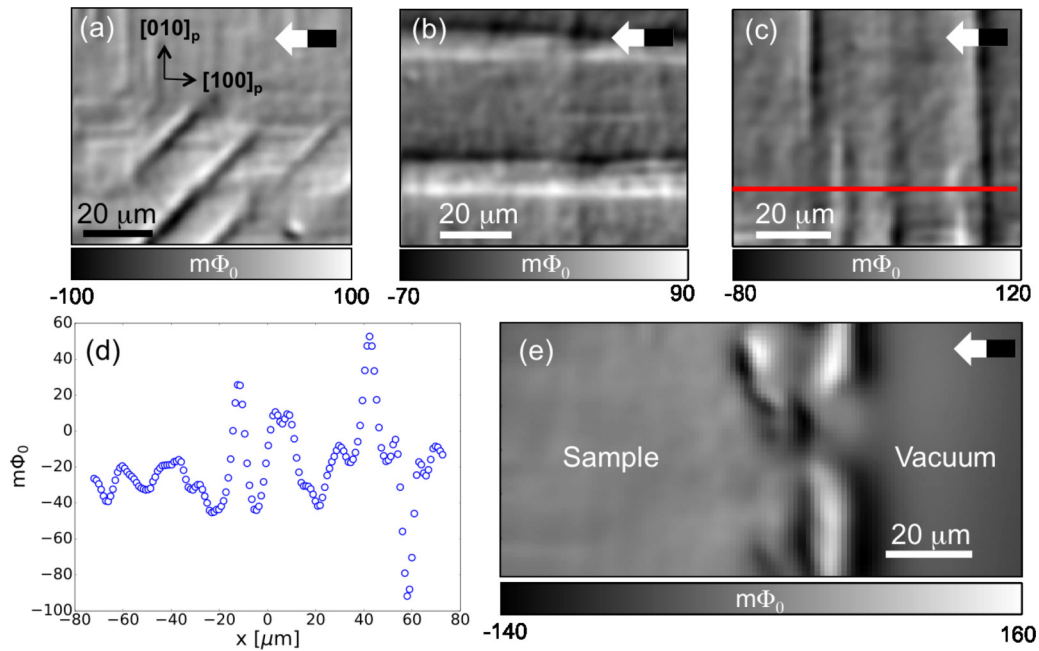


FIG. 2. Representative magnetometry images of EuS grown on STO showing modulated magnetic features that point primarily along the (a) [110]<sub>p</sub>, (b) [010]<sub>p</sub>, and (c) [100]<sub>p</sub> STO crystallographic axes. Black and white arrows show the direction of the training field. (d) A line cut of image (c), shown as the red line. (e) The edge of the sample, which allows us to determine the STO pseudocubic axes labeled in (a).

and [010]<sub>p</sub> directions. The fact that the observed magnetic features align exactly with these twin planes strongly suggests that the EuS magnetism is related to the STO tetragonal domain structure.

These images cannot describe the orientation of the spins contributing to the observed magnetic features because both in-plane and out-of-plane spins contribute to the z component of the magnetic field. However, any spatial variation in the density or the orientation of the spins would be detected and quantified by a scalar magnetic flux. Furthermore, the point-spread function of the SQUID pickup loop dictates the spatial resolution; any magnetic feature less than ≈3 μm is considered resolution limited.

We quantitatively compared the measured magnetic flux at the edge of the sample with the expected magnetic flux for a given EuS magnetization density. The mean magnetic flux magnitude of a line cut through the edge of the sample was ≈80 mΦ<sub>0</sub>, where Φ<sub>0</sub> =  $\frac{h}{2e}$  is the superconducting flux

quantum. To compute the expected magnetic flux, we first compute the magnetization density. Taking the parameters of the EuS to be 28μ<sub>B</sub>/unit cell with a lattice constant of 0.59 nm [1] and a film thickness of 5 nm, we calculate an expected flux signal of approximately 200 mΦ<sub>0</sub> [45], which is substantially larger than our measured signal at the edge. We attribute this difference to the domain structure on smaller length scales than our spatial resolution, which reduces the total signal.

To determine the relative size of the observed magnetic modulation, we compared the peak-to-peak flux signal of the features to the flux signal at the edge of the sample. Taking a line cut of Fig. 2(c) [shown in Fig. 2(d)], we measured the mean peak-to-peak magnetic flux of the modulation for five peaks to be ≈55 mΦ<sub>0</sub> through the SQUID pickup loop. This magnetic flux is ≈65% of the flux signal at the edge, indicating that the observed spatial ferromagnetic variations are substantial.

The training field polarizes some of the spins along a specific direction, and to characterize how the spin polarization

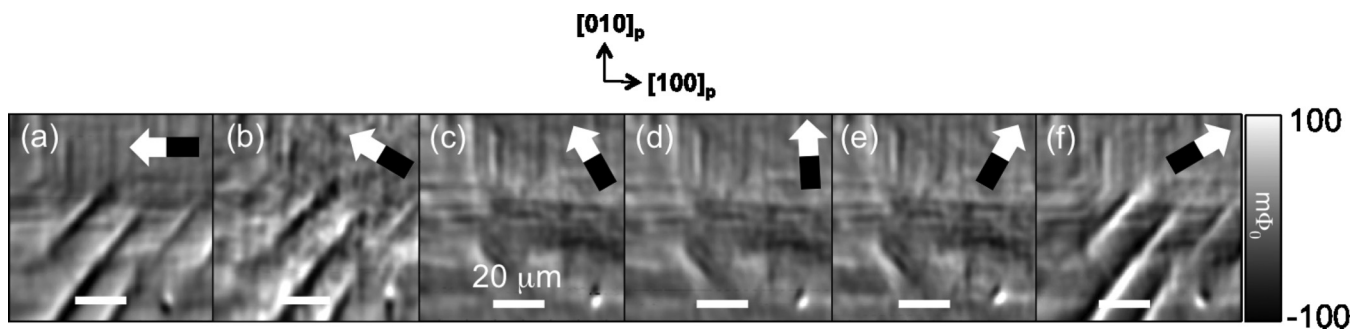


FIG. 3. Magnetometry dependence on the in-plane field training angle. Before acquiring each image, we thermal cycled the sample to 30 K, well above the Curie temperature of EuS, and cooled it with a 13-G field in the direction specified by the arrow. With respect to the [100]<sub>p</sub> direction, the angle of the training field is (a) 180°, (b) 150°, (c) 120°, (d) 90°, (e) 60°, and (f) 30°.

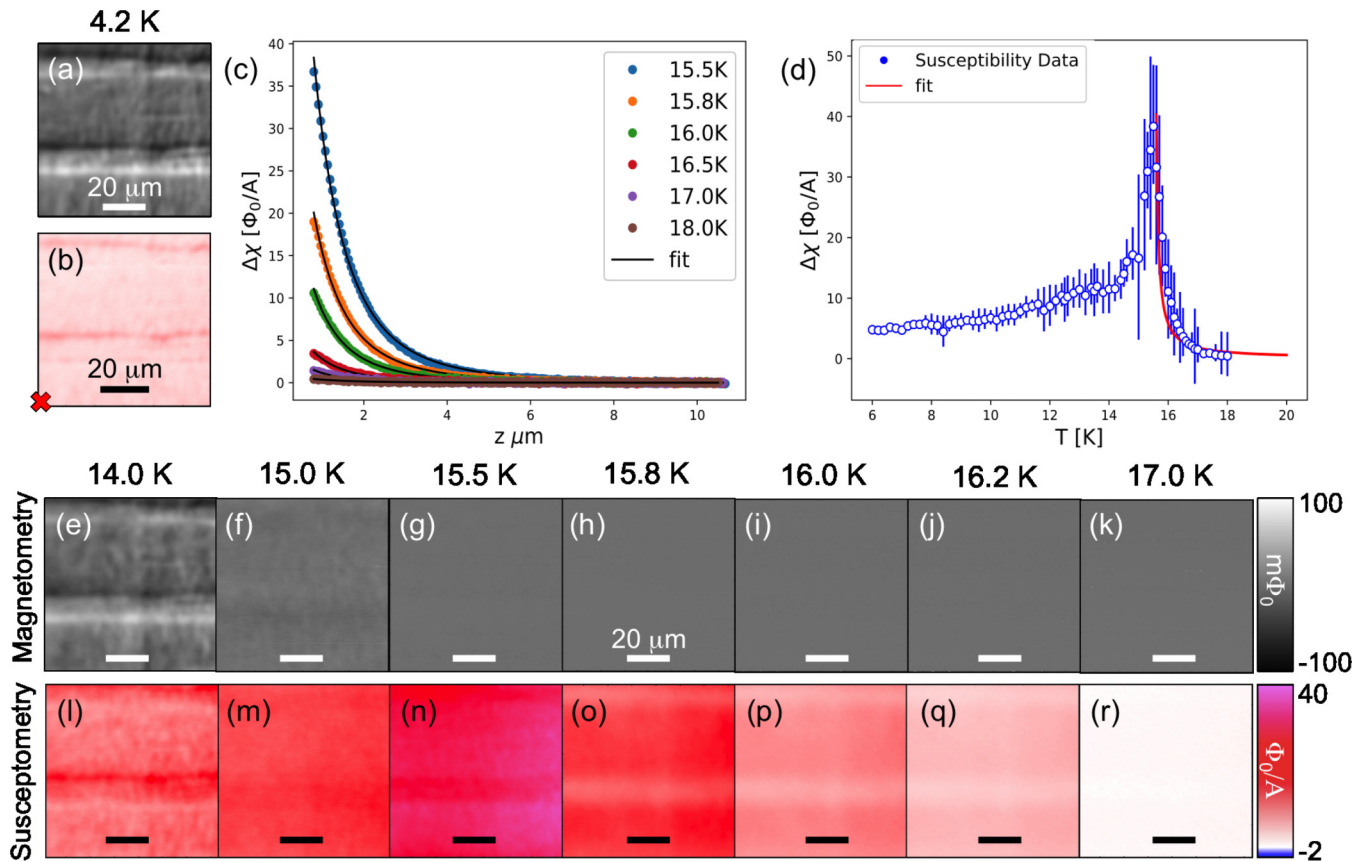


FIG. 4. Temperature dependence of the ferromagnetism and the susceptibility to determine the Curie temperature  $T_C$ . (a) Magnetometry image reproduced from Fig. 2(b), plotted with (b) the corresponding susceptibility image at 4.2 K. We performed susceptibility touchdowns as a function of the temperature at the location marked with the red X in (b). (c) Representative touchdowns showing how the susceptibility changes with the temperature close to and away from  $T_C$ . The height  $z$  is defined as the separation between the SQUID substrate and the sample surface. (d) Plot of the fitted susceptibility at  $z = 0$  with the temperature, including error bars as determined by bootstrapping. The susceptibility diverges, indicative of a paramagnetic-to-ferromagnetic phase transition. The paramagnetism above the Curie temperature is fit to a Curie-Weiss law with  $T_C = 15.4$  K. (e–k) Magnetometry and (l–r) susceptibility images as a function of the temperature. The paramagnetism above the fitted Curie temperature is spatially inhomogeneous, similar to the large ferromagnetic features below the Curie temperature at 4.2 K.

direction affects the formation of these magnetic features, we examined the dependence of the magnetic configuration on the in-plane training field direction (Fig. 3). Before acquiring each image, we thermal cycled the sample to 30 K, well above the expected Curie temperature of 16 K, and retrained the sample in a 13-G field with different in-plane orientations. The magnetic features parallel to the  $[100]_p$  and  $[010]_p$  directions were independent of the training field direction, but the large magnetic features parallel to the  $[110]_p$  direction disappeared for certain angles. This observation shows that the spin polarization orientation plays a role in the formation or visibility of these features.

To determine the Curie temperature  $T_C$ , we applied a 500- $\mu$ A ac current ( $f = 514$  Hz) to the field coil and performed a series of touchdowns to quantify the change in susceptibility with temperature. We performed touchdowns at the red X [Figs. 4(a) and 4(b)], and we observed the susceptibility diverge as the temperature approached 15.5 K, indicating a ferromagnetic-to-paramagnetic transition [Fig. 4(c)]. When we plotted the measured susceptibility when the SQUID was closest to the sample versus the temperature [Fig. 4(d)], we detected a divergence around 15.5 K associated

with a ferromagnetic-to-paramagnetic transition. The error bars in Fig. 4(d) were determined by fitting bootstrapped touchdown data shown in Fig. 4(c) using the form for the susceptibility of a thin isotropic and monodomain paramagnet [45,49]. The touchdown fits without bootstrapping shown in Fig. 4(c) clearly deviated from the measured data, perhaps because of uncertainty in the height calibration or unaccounted piezoelectric drift. The susceptibility for  $T > T_C$  measures the paramagnetic response of the sample, which we fit to the Curie-Weiss law  $\chi(T) = \frac{C}{T - T_C}$  [Fig. 4(d)], where  $T_C$  is the Curie temperature and  $C$  is a proportionality constant, with  $T_C$  and  $C$  the only free parameters. The Curie-Weiss law does not perfectly capture the data [Fig. 4(d)], perhaps due to the height uncertainty and possible fluctuations close to  $T_C$  [2,12,13], but it does find the divergencelike peak in the paramagnetism. However, this fit yielded a fitted  $T_C = 15.4$  K, which is similar to previously reported values for EuS [1]. As a check on our fitted  $T_C$ , we imaged the ferromagnetism with the temperature [Figs. 4(e)–4(k)] and found that the signal became indistinguishable from noise around 15.5 K, consistent with the absence of ferromagnetic order. Images of the paramagnetism [Figs. 4(l)–4(r)] above the Curie temperature showed spatially

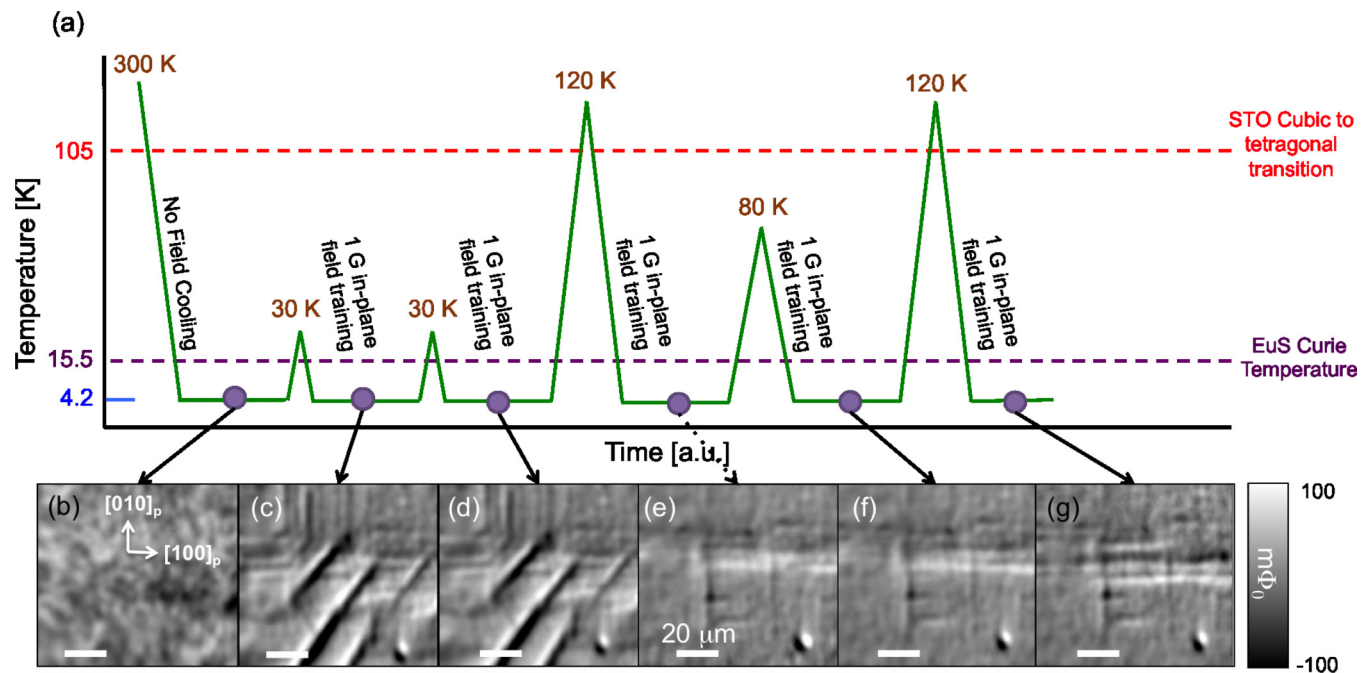


FIG. 5. Ferromagnetic spatial variations upon thermal cycling reveal a relationship between the magnetic structure and the STO structural phase transition. (a) Thermal history of one region; all images were taken at 4.2 K. (b) The sample was cooled from room temperature without field training, showing resolution-limited domains. (c) The sample was warmed above the Curie temperature of the EuS (30 K) and field trained with 1 G, revealing a striplike magnetic configuration. The sample was then thermal cycled to (d) 30 K, (e) 120 K, (f) 80 K, and (g) 120 K, each cooled with a 1-Gauss. From (d) to (e) and from (f) to (g), there are changes in the magnetic configuration corresponding to thermal cycling above the STO cubic-to-tetragonal phase transition, but the magnetic configuration does not change otherwise, suggesting that the observed magnetic configuration is related to the STO structural phase transition.

varying features similar to those shown by the ferromagnetism, suggesting that the paramagnetism is modified by a similar mechanism as the ferromagnetism.

To demonstrate that the observed magnetic behavior is due to the STO tetragonal structure, we studied how the ferromagnetic configuration changed with the thermal history [Fig. 5(a)]. Without any field training, the magnetometry image shows resolution-limited magnetic domains similar to SQUID measurements on conventional ferromagnets [50] [Fig. 5(b)], and we observe the magnetic striations when training in a small field [Fig. 5(c)]. Upon thermal cycling above the Curie temperature to 30 K [Fig. 5(d)], the magnetic configuration does not show any distinct changes, suggesting that the magnetic configuration is predetermined even before the EuS becomes ferromagnetic. However, during thermal cycling above 105 K, the magnetic configuration was substantially modified [compare Figs. 5(d) and 5(e) and Figs. 5(f) and 5(g)]. Similarly to the magnetic features in Fig. 2, all the features observed from thermal cycling point only along directions that intersect with twin planes, namely,  $[100]_p$  and  $[010]_p$ . Because the magnetic features only changed during thermal cycling above the STO cubic-to-tetragonal transition, and because the features only pointed along twin plane directions, we conclude that the configuration of the EuS magnetism is coupled to the configuration of the STO twin structure. With this information, we conclude that the reason the magnetic structures in Figs. 5(d) and 5(e) show so much contrast is that the STO forms tetragonal domains, and thermal cycling above the transition temperature will cause the domains to reshuffle.

Because the real-space magnetic features are correlated with the underlying transition, the magnetic images should reshuffle as well. Because there is no external stain in the system, thermal cycling should not show any directional dependence.

We now discuss possible origins of the observed features. One possible explanation is that the modulated magnetism is due to the topography on the surface of STO from the twin planes. Scanning single-electron transistor studies have shown that the STO structural transition causes the twin boundaries between tetragonal domains to have a topographical kink with a change in slope of  $\tan \alpha = \frac{1}{1000}$  [43]. For larger boundaries between tetragonal domains, such as 15–20  $\mu\text{m}$ , that kink can lead to topological variations as great as 5 nm [43]. Because the EuS is epitaxially grown on STO, the EuS could also experience this topography. The SQUID would measure a spatially dependent magnetic flux due to the height variation. We simulate the spatial magnetic flux from this topographical variation and find that this effect produces a spatially dependent magnetization that is two orders of magnitude smaller than the measured magnetic spatial variations [45]. We conclude that the surface topography does not fully explain our results.

The coupling between the EuS magnetism and the STO tetragonal structure may be magnetoelastic in origin. EuS may experience a spatially dependent strain due to STO twin formation that may alter the magnetic anisotropy along the twin boundaries giving rise to the features observed in this work. Magnetic anisotropy is determined by magnetocrystalline energy and magnetoelastic energy, and we can

TABLE I. For different strains  $\epsilon$  we compare the magnetoelastic energy  $K_{\text{me,max}}(x, y)$ , which can vary in space with the magnetocrystalline energy  $K_{\text{mc}}$ .

$\epsilon_{[100]_p}$	$K_{\text{me,max}}(x, y)$ ( $10^4$ erg/cm $^3$ )	$K_{\text{me,max}}/K_{\text{mc}}$
$10^{-5}$	$\simeq 0.018$	0.0075
$10^{-4}$	$\simeq 0.18$	0.075
$10^{-3}$	$\simeq 1.8$	0.75
$10^{-2}$	$\simeq 18$	7.5

compare these two energy scales to determine which has a stronger influence on the anisotropy. The magnetocrystalline energy for a cubic system is expressed as  $E_{\text{mc}} = K_{\text{mc}}(\alpha_1^2\alpha_2^2 + \alpha_2^2\alpha_3^2 + \alpha_3^2\alpha_1^2)$ , where  $K_{\text{mc}} = 2.4 \times 10^4$  erg/cm $^3$  and  $\alpha_i$  are the directional cosines of the magnetization [51]. The magnetoelastic energy is expressed as  $E_{\text{me}} = -K_{\text{me}}(x, y)\alpha_k\alpha_l$ , where  $K_{\text{me}} = \frac{3}{2}\lambda_{ijkl}\sigma_{ij}(x, y)$ ,  $\lambda_{ijkl}$  are the magnetostriction coefficients, and  $\sigma_{ij}(x, y)$  is the stress from the STO twins in the  $x$ - $y$  plane. Along the  $[100]_p$  direction, the highest value of  $K_{\text{me}}(x, y)$  is when the strain is along the  $[100]_p$  direction, which is expressed as  $K_{\text{me,max}}(x, y) = \frac{3}{2}\lambda_{[100]_p}\sigma_{[100]_p}(x, y) = \frac{3}{2}\lambda_{[100]_p}c_{11}\epsilon_{[100]_p}(x, y)$ , where  $c_{11}$  is the elastic modulus along the  $[100]_p$  direction and  $\epsilon(x, y)$  is the strain. Using values from the literature [52,53],  $\lambda_{[100]_p} \simeq 10^{-5}$  and  $c_{11} \simeq 120$  GPa, so  $K_{\text{me,max}}(x, y) = 1.8 \times 10^7\epsilon(x, y)$  erg/cm $^3$ . Note that  $\lambda_{[100]_p}$  was experimentally determined for EuO, a related Eu chalcogenide.

To complete this calculation, we need to know  $\epsilon(x, y)$ . It is noteworthy that the x-ray diffraction measurements in Fig. 1(e) show that the out-of-plane lattice constant for 5 nm of EuS grown on STO has a strain of  $\epsilon = 2 \times 10^{-2}$  at room temperature. However, this measured strain neglects how strain may vary spatially from twin formation, and calculating or experimentally determining the amount of strain for a thin film spatially is difficult. Instead, we remain agnostic as to how much strain is actually being applied, so we compare the magnetoelastic energy with the magnetocrystalline energy for a variety of strains, as listed in Table I. For small strains, the magnetocrystalline energy dominates, so the magnetoelastic energy will have a negligible effect on the anisotropy. However, for large strains that may occur from twin boundaries, the magnetoelastic energy will strongly influence the anisotropy, which may give rise to the spatially varying magnetic structure observed in this work.

Strain from twin formation in STO has been observed to alter the magnetic properties of  $\text{La}_{2/3}\text{Ca}_{1/3}\text{MnO}_3$  (LCMO) and  $\text{La}_{0.7}\text{Ca}_{0.3}\text{MnO}_3$  (LSMO) grown on STO, perhaps also arising

from a magnetoelastic origin. Bulk magnetic measurements on LCMO grown on STO [54] and LSMO grown on STO [55] show changes in magnetization during cooling below the 105 K transition temperature, and micron-scale magnetic features similar to those reported in Fig. 2 were observed via magneto-optic measurements [56]. The conclusion of that work is that strain from the STO twin structure causes a small out-of-plane rotation of the magnetic moments, which produces the observed spatial features in magnetism. However, this explanation is not necessarily applicable to this work because the origins of the magnetism in LCMO and EuS are different (respectively, double exchange [57] and indirect exchange [58]), and we have no evidence that the EuS magnetic moments have an out-of-plane component.

Much more information is needed to confirm a magnetoelastic argument. First, one could perform x-ray diffraction measurements as a function of the temperature through the cubic-to-tetragonal phase transition to see how the EuS lattice constant changes, although these changes will be over a large length scale so it would still be hard to map these measurements to the micron-scale SQUID results. Second, one could apply controlled uniaxial strain to the EuS/STO heterostructure and measure how the magnetism changes with a scanning SQUID or magneto-optic technique. Finally, density functional theory calculations could shed light on how a compressed lattice constant affects magnetism in EuS.

In conclusion, here we have shown that the STO tetragonal structure modifies the magnetism of an epitaxially coupled thin film of EuS. Understanding how structural changes influence magnetism may shed light on the fundamental basis of exchange interactions and lead to the development of new and interesting systems. Thus, these changes and their impact on magnetism need to be considered when constructing devices that require homogeneous magnetic exchange.

The authors thank Adrian G. Swartz, Zheng Cui, Hilary Noad, Eric M. Spanton, Maxwell C. Shapiro for useful discussions as well as Sean Hart and Yuri Suzuki for assistance with the manuscript. This work was supported by FAME, one of six centers of STARnet, a Semiconductor Research Corporation program sponsored by MARCO and DARPA. The SQUID microscope and sensors used were developed with support from the NSF-sponsored Center for Probing the Nanoscale at Stanford, NSF-NSEC Grant No. 0830228, and from NSF Grant No. IMR-MIP 0957616. F.K. and J.S.M. acknowledge the support from NSF Grant No. DMR-1207469, ONR Grant Nos. N00014-13-1-0301 and N00014-16-1-2657, and the STC Center for Integrated Quantum Materials under NSF Grant No. DMR-1231319. N.G. and F.K. are supported by the STC Center for Integrated Quantum Materials under NSF Grant No. DMR-1231319.

- [1] A. Mauger and C. Godart, *Phys. Rep.* **141**, 51 (1986).  
 [2] H. Idzuchi, Y. Fukuma, H. S. Park, T. Matsuda, T. Tanigaki, S. Aizawa, M. Shirai, D. Shindo, and Y. Otani, *Appl. Phys. Express* **7**, 113002 (2014).

- [3] J. Kötzer and M. Muschke, *Phys. Rev. B* **34**, 3543 (1986).  
 [4] T. Nagahama, T. S. Santos, and J. S. Moodera, *Phys. Rev. Lett.* **99**, 016602 (2007).

- [5] P. LeClair, J. Ha, H. Swagten, J. Kohlhepp, C. Van de Vin, and W. De Jonge, *Appl. Phys. Lett.* **80**, 625 (2002).
- [6] G.-X. Miao, M. Müller, and J. S. Moodera, *Phys. Rev. Lett.* **102**, 076601 (2009).
- [7] J. S. Moodera, T. S. Santos, and T. Nagahama, *J. Phys.: Condens. Matter* **19**, 165202 (2007).
- [8] X. Hao, J. S. Moodera, and R. Meservey, *Phys. Rev. B* **42**, 8235 (1990).
- [9] J. S. Moodera, X. Hao, G. A. Gibson, and R. Meservey, *Phys. Rev. Lett.* **61**, 637 (1988).
- [10] H. G. Bohn, A. Kollmar, and W. Zinn, *Phys. Rev. B* **30**, 6504 (1984).
- [11] L. Passell, O. Dietrich, and J. Als-Nielsen, *Phys. Rev. B* **14**, 4897 (1976).
- [12] J. Als-Nielsen, O. Dietrich, W. Kunmann, and L. Passell, *Phys. Rev. Lett.* **27**, 741 (1971).
- [13] J. Als-Nielsen, O. Dietrich, and L. Passell, *Phys. Rev. B* **14**, 4908 (1976).
- [14] O. Dietrich, J. Als-Nielsen, and L. Passell, *Phys. Rev. B* **14**, 4923 (1976).
- [15] P. Wei, F. Katmis, B. A. Assaf, H. Steinberg, P. Jarillo-Herrero, D. Heiman, and J. S. Moodera, *Phys. Rev. Lett.* **110**, 186807 (2013).
- [16] C. Lee, F. Katmis, P. Jarillo-Herrero, J. S. Moodera, and N. Gedik, *Nat. Commun.* **7**, 12014 (2016).
- [17] H. Zhang, C. X. Liu, X. L. Qi, X. Dai, Z. Fang, and S.-C. Zhang, *Nat. Phys.* **5**, 438 (2009).
- [18] Y. Zhang, K. He, C.-Z. Chang, C.-L. Song, L.-L. Wang, X. Chen, J.-F. Jia, Z. Fang, X. Dai, W.-Y. Shan *et al.*, *Nat. Phys.* **6**, 584 (2010).
- [19] M. Bianchi, D. Guan, S. Bao, J. Mi, B. B. Iversen, P. D. King, and P. Hofmann, *Nat. Commun.* **1**, 128 (2010).
- [20] D. Kim, S. Cho, N. P. Butch, P. Syers, K. Kirshenbaum, S. Adam, J. Paglione, and M. S. Fuhrer, *Nat. Phys.* **8**, 459 (2012).
- [21] W. Zhang, R. Yu, H.-J. Zhang, X. Dai, and Z. Fang, *New J. Phys.* **12**, 065013 (2010).
- [22] F. Katmis, V. Lauter, F. S. Nogueira, B. A. Assaf, M. E. Jamer, P. Wei, B. Satpati, J. W. Freeland, I. Eremin, D. Heiman *et al.*, *Nature* **533**, 513 (2016).
- [23] M. Z. Hasan and C. L. Kane, *Rev. Mod. Phys.* **82**, 3045 (2010).
- [24] J. D. Sau, R. M. Lutchyn, S. Tewari, and S. Das Sarma, *Phys. Rev. Lett.* **104**, 040502 (2010).
- [25] X.-L. Qi, T. L. Hughes, and S.-C. Zhang, *Phys. Rev. B* **78**, 195424 (2008).
- [26] A. M. Essin, J. E. Moore, and D. Vanderbilt, *Phys. Rev. Lett.* **102**, 146805 (2009).
- [27] X.-L. Qi, R. Li, J. Zang, and S.-C. Zhang, *Science* **323**, 1184 (2009).
- [28] R. B. Laughlin, *Phys. Rev. Lett.* **50**, 1395 (1983).
- [29] C.-Z. Chang, J. Zhang, X. Feng, J. Shen, Z. Zhang, M. Guo, K. Li, Y. Ou, P. Wei, L.-L. Wang *et al.*, *Science* **340**, 167 (2013).
- [30] Q.-Y. Wang, Z. Li, W.-H. Zhang, Z.-C. Zhang, J.-S. Zhang, W. Li, H. Ding, Y.-B. Ou, P. Deng, K. Chang *et al.*, *Chin. Phys. Lett.* **29**, 037402 (2012).
- [31] X. Wu, D. Dijkkamp, S. Ogale, A. Inam, E. Chase, P. Miceli, C. Chang, J. Tarascon, and T. Venkatesan, *Appl. Phys. Lett.* **51**, 861 (1987).
- [32] J.-F. Ge, Z.-L. Liu, C. Liu, C.-L. Gao, D. Qian, Q.-K. Xue, Y. Liu, and J.-F. Jia, *Nat. Mater.* **14**, 285 (2015).
- [33] H. Sun, W. Tian, X. Pan, J. H. Haeni, and D. G. Schlom, *Appl. Phys. Lett.* **84**, 3298 (2004).
- [34] J. Jiang, X. Pan, W. Tian, C. Theis, and D. Schlom, *Appl. Phys. Lett.* **74**, 2851 (1999).
- [35] A. D. Caviglia, M. Gabay, S. Gariglio, N. Reyren, C. Cancellieri, and J.-M. Triscone, *Phys. Rev. Lett.* **104**, 126803 (2010).
- [36] S. N. Klimin, J. Tempere, D. van der Marel, and J. T. Devreese, *Phys. Rev. B* **86**, 045113 (2012).
- [37] C. Koonce, M. L. Cohen, J. Schooley, W. Hosler, and E. Pfeiffer, *Phys. Rev.* **163**, 380 (1967).
- [38] A. Ohtomo and H. Hwang, *Nature* **427**, 423 (2004).
- [39] S. Thiel, G. Hammerl, A. Schmehl, C. Schneider, and J. Mannhart, *Science* **313**, 1942 (2006).
- [40] N. Reyren, S. Thiel, A. Caviglia, L. F. Kourkoutis, G. Hammerl, C. Richter, C. Schneider, T. Kopp, A.-S. Rüetschi, D. Jaccard *et al.*, *Science* **317**, 1196 (2007).
- [41] R. Cowley, *Phys. Rev.* **134**, A981 (1964).
- [42] B. Kalisky, E. M. Spanton, H. Noad, J. R. Kirtley, K. C. Nowack, C. Bell, H. K. Sato, M. Hosoda, Y. Xie, Y. Hikita *et al.*, *Nat. Mater.* **12**, 1091 (2013).
- [43] M. Honig, J. A. Sulpizio, J. Drori, A. Joshua, E. Zeldov, and S. Ilani, *Nat. Mater.* **12**, 1112 (2013).
- [44] H. Noad, E. M. Spanton, K. C. Nowack, H. Inoue, M. Kim, T. A. Merz, C. Bell, Y. Hikita, R. Xu, W. Liu *et al.*, *Phys. Rev. B* **94**, 174516 (2016).
- [45] See Supplemental Material at <http://link.aps.org/supplemental/10.1103/PhysRevMaterials.1.074406> for measurements on additional samples, training-field dependence on the modulated magnetism, magnetic flux simulations exploring potential origins of the modulated ferromagnetism, and how paramagnetism is quantified.
- [46] E. H. Brandt, *Phys. Rev. B* **72**, 024529 (2005).
- [47] J. R. Kirtley, L. Paulius, A. J. Rosenberg, J. C. Palmstrom, C. M. Holland, E. M. Spanton, D. Schiessl, C. L. Jermain, J. Gibbons, Y.-K.-K. Fung *et al.*, *Rev. Sci. Instrum.* **87**, 093702 (2016).
- [48] M. E. Huber, N. C. Koshnick, H. Bluhm, L. J. Archuleta, T. Azua, P. G. Björnsson, B. W. Gardner, S. T. Halloran, E. A. Lucero, and K. A. Moler, *Rev. Sci. Instrum.* **79**, 053704 (2008).
- [49] J. Kirtley, B. Kalisky, J. Bert, C. Bell, M. Kim, Y. Hikita, H. Hwang, J. Ngai, Y. Segal, F. Walker *et al.*, *Phys. Rev. B* **85**, 224518 (2012).
- [50] T. Higgs, S. Bonetti, H. Ohldag, N. Banerjee, X. Wang, A. Rosenberg, Z. Cai, J. Zhao, K. Moler, and J. Robinson, *Sci. Rep.* **6**, 30092 (2016).
- [51] M. Franzblau, G. E. Everett, and A. Lawson, *Phys. Rev.* **164**, 716 (1967).
- [52] B. Argyle and N. Miyata, *Phys. Rev.* **171**, 555 (1968).
- [53] Q. Liu and F. Peng, *Chin. J. Chem. Phys.* **27**, 387 (2014).
- [54] M. Ziese, I. Vrejoiu, A. Setzer, A. Lotnyk, and D. Hesse, *New J. Phys.* **10**, 063024 (2008).
- [55] E. Wahlström, F. Macià, J. E. Boschker, Å. Monsen, P. Nordblad, R. Mathieu, A. D. Kent, and T. Tybell, *New J. Phys.* **19**, 063002 (2017).
- [56] V. K. Vlasko-Vlasov, Y. K. Lin, D. J. Miller, U. Welp, G. W. Crabtree, and V. I. Nikitenko, *Phys. Rev. Lett.* **84**, 2239 (2000).
- [57] K. Ghosh, C. J. Lobb, R. L. Greene, S. G. Karabashev, D. A. Shulyatev, A. A. Arsenov, and Y. Mukovskii, *Phys. Rev. Lett.* **81**, 4740 (1998).
- [58] I. N. Goncharenko and I. Mirebeau, *Phys. Rev. Lett.* **80**, 1082 (1998).